ResearchGate

See discussions, stats, and author profiles for this publication at: https://www.researchgate.net/publication/273676893

Refining Space Object Radiation Pressure Modeling with Bidirectional Reflectance Distribution Functions

Article *in* Journal of Guidance, Control, and Dynamics · January 2014

DOI: 10.2514/1.60577

CITATIONS
43

READS
1,930

7 authors, including:

Richard Linares
Massachusetts Institute of Technology
297 PUBLICATIONS **3,580** CITATIONS

SEE PROFILE

John Crassidis
University at Buffalo, State University of New York
274 PUBLICATIONS **11,381** CITATIONS

SEE PROFILE

Marek Ziebart
University College London
81 PUBLICATIONS **2,434** CITATIONS

SEE PROFILE

Moriba Jah
University of Texas at Austin
144 PUBLICATIONS **2,455** CITATIONS

SEE PROFILE

All content following this page was uploaded by Moriba Jah on 13 July 2015.

The user has requested enhancement of the downloaded file.

JOURNAL OF GUIDANCE, CONTROL, AND DYNAMICS
Vol. 37, No. 1, January–February 2014

Refining Space Object Radiation Pressure Modeling with Bidirectional Reflectance Distribution Functions

Charles J. Wetterer*
Pacific Defense Solutions, Kihei, Hawaii 96753
Richard Linares† and John L. Crassidis‡
University at Buffalo, State University of New York, Amherst, New York 14260
Thomas M. Kelecy§
Boeing LTS, Colorado Springs, Colorado 80919
Marek K. Ziebart¶
University College London, London, England WC1E 6BT, United Kingdom
Moriba K. Jah**
U.S. Air Force Research Laboratory, Space Vehicles Directorate, Kirtland Air Force Base, New Mexico 87117
and
Paul J. Cefola††
University at Buffalo, State University of New York, Amherst, New York 14260

DOI: 10.2514/1.60577

High-fidelity orbit propagation requires detailed knowledge of the solar radiation pressure on a space object. The solar radiation pressure depends not only on the space object's shape and attitude, but also on the absorption and reflectance properties of each surface on the object. These properties are typically modeled in a simplistic fashion, but are here described by a surface bidirectional reflectance distribution function. Several analytic bidirectional reflectance distribution function models exist, and are typically complicated functions of illumination angle and material properties represented by parameters within the model. In general, the resulting calculation of the solar radiation pressure would require a time-consuming numerical integration. This might be impractical if multiple solar radiation pressure calculations are required for a variety of material properties in real time; for example, in a filter where the particular surface parameters are being estimated. This paper develops a method to make accurate and precise solar radiation pressure calculations quickly for some commonly used analytic bidirectional reflectance distribution functions. In addition, other radiation pressures exist, including Earth albedo/Earth infrared radiation pressure, and thermal radiation pressure from the space object itself, and are influenced by the specific bidirectional reflectance distribution function. A description of these various radiation pressures and a comparison of the magnitude of the resulting accelerations at various orbital heights and the degree to which they affect the space object's orbit are also presented. Significantly, this study suggests that, for space debris whose interactions with electro-magnetic radiation are described accurately with a bidirectional reflectance distribution function, then hitherto unmodeled torques would account for rotational characteristics affecting both tracking signatures and the ability to predict the orbital evolution of the objects.

Downloaded by AFRL/DII on January 22, 2014 | http://arc.aiaa.org | DOI: 10.2514/1.60577

I. Introduction

OBSERVATIONS made on uncontrolled high area-to-mass ratio (HAMR) debris objects in near geosynchronous orbit (GEO) indicate they can have apparent effective area-to-mass ratio (AMR) values ranging anywhere from 0.1 to tens of meters squared per kilogram [1]. Only a subset of these observations produced this result out of many more detections that remain unassociated to unique objects. In other words, there is an as-of-yet unquantified population of space objects (SOs) near the GEO region due to an inability in converting optical detections into predictable orbits that allow proper data association. Because the detections obtained for any specific object are sparse, the modeling of the dynamic behavior of the SO is critical for successful object reacquisition and data association. Previous analyses have shown that HAMR objects have AMR values that vary with time and produce significant variations over relatively short periods of time (days to weeks) [2,3]. This is likely due to stochastic solar radiation pressure (SRP) accelerations resulting from time varying solar illumination due to orientation changes with respect to the sun and solar eclipsing periods. These in turn result in time varying reflective and emissive accelerations that are difficult to predict. This intuitively makes sense given that these objects are uncontrolled and their motion is driven by their interaction with a dynamic space environment (i.e., processes that are both deterministic and stochastic). Reference [4] presents a detailed SRP

Received 3 October 2012; accepted for publication 5 April 2013; published online 18 October 2013. Copyright © 2013 by the American Institute of Aeronautics and Astronautics, Inc. The U.S. Government has a royalty-free license to exercise all rights under the copyright claimed herein for Governmental purposes. All other rights are reserved by the copyright owner. Copies of this paper may be made for personal or internal use, on condition that the copier pay the $10.00 per-copy fee to the Copyright Clearance Center, Inc., 222 Rosewood Drive, Danvers, MA 01923; include the code 1533-3884/13 and $10.00 in correspondence with the CCC.

*Principal Scientist, 1300 N. Holopono St. Suite116; jack.wetterer@pacificds.com.

†Graduate Student, Department of Mechanical and Aerospace Engineering; linares2@buffalo.edu. Student Member AIAA.

‡CUBRC Professor in Space Situational Awareness, Department of Mechanical and Aerospace Engineering; johnc@buffalo.edu. Associate Fellow AIAA.

§Senior Scientist, 5555 Tech Center Dr., Suite 400; Thomas.M.Kelecy@boeing.com.

¶Professor of Space Geodesy, Department of Civil, Environmental and Geomatic Engineering; m.ziebart@ucl.ac.uk.

**Senior Aerospace Engineer. Associate Fellow AIAA.

††Adjunct Professor, Department of Mechanical and Aerospace Engineering; also Consultant in Aerospace Systems, Spaceflight Mechanics, and Astrodynamics; paulcefo@buffalo.edu. Associate Fellow AIAA.

Downloaded by AFRL/DII on January 22, 2014 | http://arc.aiaa.org | DOI: 10.2514/1.60577

formulation that models the time varying orientation and surface thermal characteristics of HAMR objects in space, and quantifies the perturbation errors due to a variety of modeling assumptions in the determination and prediction of the orbits of these objects. It is shown that the errors due to the mismodeling of thermal emissions are large enough to result in significant errors in the orbit predictions and, in particular, can result in unbalanced accelerations in directions orthogonal to the object–sun line. The analysis examined the sensitivity to the lack of a priori knowledge of attitude, shape, or materials. The perturbations resulting from unmodeled dynamics due to inadequate shape/attitude knowledge and radiation pressure models explain, at least partly, the discrepancies between the vast literature on theoretical long-term orbital histories, actual observed behavior for a subset of optical detections that have been successfully correlated to unique objects, and the lack of success in adjudicating the remainder of optical detections.

The physical correlation between the SO's shape/attitude and its orbital position due to the various nongravitational forces and torques, such as the SRP, which depend on shape and attitude, can be used to determine physical characteristics about the object. For example, with angles data alone, it is possible to infer an effective albedo area to mass ratio as shown in [5,6]. The observability of this parameter is due to the SRP perturbation effects experienced by the SO indirectly observed in the line-of-sight data. The surface reflectance parameters, such as albedo, influencing the SO's dynamics are the same surface reflectance parameters that determine the object's observed brightness. This is the physical link that enables both angles (astrometric line-of-sight) and brightness (photometric flux intensity) measurements to be fused and exploited for the purpose of simultaneous orbit, attitude, and shape determination of an SO. It is theoretically demonstrated that simultaneously processing both astrometric and photometric measurements enables shape and attitude estimates that leads to improved orbit propagation [7].

High-fidelity orbit propagation is necessary to reacquire a HAMR object over significant temporal sparseness in observations. For this process to yield accurate results, however, the model used to calculate the brightness of the SO must be physically consistent with the model used to calculate the SRP and other nongravitational forces and torques. Brightness models are based on the surface bidirectional reflectance distribution function (BRDF), where BRDFs define how the diffuse and specular components of light are reflected from the surface. However, SRP calculations typically use an idealized BRDF in developing the characteristic equation and, in some cases, a simplified shape model (e.g., a diffuse cannonball). In this paper, the SRP calculation is reconciled with more physically realistic BRDF functions.

The work presented here aims to show the importance of properly accounting for the BRDF when considering radiation pressure accelerations. First, the dependence of the SRP on the BRDF is demonstrated in Sec. II and descriptions of two commonly used BRDFs are presented in Sec. III. The correction factors required in the procedure used to reconcile the SRP to the BRDF are then calculated in Sec. IV. Other radiation pressures, the Earth–albedo/Earth–infrared radiation pressure (ERP), and the thermal radiation pressure (TRP) are described in Sec. V along with how these are reconciled with the BRDF. For the TRP, this requires the development of a completely new model. Finally, the deterministic orbit and attitude propagation equations used in the analysis are described in Sec. VI and a comparison of the magnitude of the various radiation pressures and the resulting propagation errors on a HAMR object is presented in Sec. VII.

II. SRP Dependence on BRDF

The BRDF (f_r) defines how light is reflected from an opaque surface with a given surface normal direction $\hat{\boldsymbol{N}}$, illumination direction $\hat{\boldsymbol{L}}$ with θ_i the normal angle from $\hat{\boldsymbol{N}}$ and ϕ_i the azimuth from the x axis, and observer direction $\hat{\boldsymbol{V}}$ with θ_r the normal angle from $\hat{\boldsymbol{N}}$ and ϕ_r the azimuth from the x axis, as shown in Fig. 1, and is given by

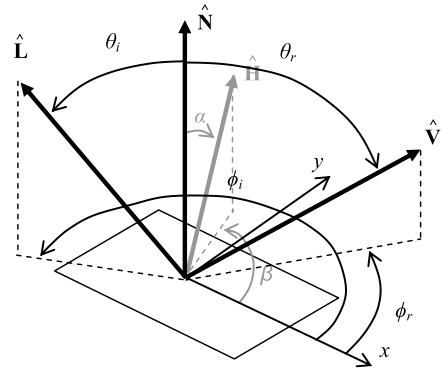

Fig. 1 The geometry of reflection.

$$f_r(\theta_i, \phi_i; \theta_r, \phi_r; \lambda) = \frac{\mathrm{d}L_r(\theta_r, \phi_r; \lambda)}{\mathrm{d}E_i(\theta_i, \phi_i; \lambda)} \tag{1}$$

where $\mathrm{d}L_r$ is the reflected radiance in $\mathrm{W \cdot m^{-2} sr^{-1}}$, $\mathrm{d}E_i$ is the irradiance in $\mathrm{W \cdot m^{-2}}$, and λ is the wavelength. The bisector vector between the illumination source and the observer is $\hat{\boldsymbol{H}} = (\hat{\boldsymbol{L}} + \hat{\boldsymbol{V}})/|\hat{\boldsymbol{L}} + \hat{\boldsymbol{V}}|$ with α the normal angle from $\hat{\boldsymbol{N}}$ and β the azimuth from the x axis. These are also shown in Fig. 1 and are used later in the BRDF models.

The acceleration caused by the SRP can be calculated by summing the individual contributions of all the constituent illuminated "facets" that make up the object, where a facet is defined as a flat surface of a particular area and surface normal direction. The acceleration is

$$\boldsymbol{a}_{\mathrm{SRP}} = -\sum_{k=1}^{N_{\mathrm{facets}}} \int_0^\infty \frac{F_i(\lambda) A_k f_k (\hat{\boldsymbol{L}} \cdot \hat{\boldsymbol{N}}_k)_+}{m_{\mathrm{so}} c} \times \left[\hat{\boldsymbol{L}} + \left(\int_0^{2\pi} \int_0^{\pi/2} f_r \cos\theta_r \hat{\boldsymbol{V}} \, \mathrm{d}\theta_r \, \mathrm{d}\phi_r \right)_k \right] \mathrm{d}\lambda \tag{2}$$

where $F_i(\lambda)$ is the solar flux (in $\mathrm{W \cdot m^{-2} nm^{-1}}$), A_k is the facet area, f_k is the fraction of the facet that is illuminated (due to self-shadowing), m_{so} is the mass of the object, c is the speed of light, N_{facets} is the total number of facets, and the BRDF for each facet is integrated over all observer directions and all wavelengths. In addition, $(x)_+ = xH(x)$ where $H(x)$ is the Heaviside step function, which is unity for positive values and zero elsewhere. The first term in parentheses in Eq. (2) is simply the acceleration resulting from the momentum exchange of the incoming photons, and the second term in parentheses is the acceleration resulting from the fraction of incoming photons reflected by the surface.

In an effort to establish a common nomenclature, the general BRDF is calculated using

$$f_r = (dR_d + sR_s) \tag{3}$$

which depends on the diffuse bidirectional reflectance R_d and the specular bidirectional reflectance R_s and the fraction of each to the total reflectance (d and s, respectively, where $d + s = 1$), which again is in and of itself a fraction of the total incoming energy.

In general, R_d and R_s are complicated functions of illumination angle and material properties represented by parameters within the particular BRDF model. For certain BRDFs, however, the integral can be solved analytically. For example, the BRDF with a Lambertian diffuse component and purely "mirror-like" specular component (where $\hat{\boldsymbol{R}} = 2(\hat{\boldsymbol{L}} \cdot \hat{\boldsymbol{N}})\hat{\boldsymbol{N}} - \hat{\boldsymbol{L}}$ is the direction of mirror-like reflection of $\hat{\boldsymbol{L}}$) is given by

$$f_r = d\left(\frac{\rho}{\pi}\right) + s\left[\frac{F_0 \delta(\hat{\boldsymbol{V}} - \hat{\boldsymbol{R}})}{\cos\theta_i}\right] \tag{4}$$

where ρ is the diffuse reflectance ($0 \le \rho \le 1$), F_0 is the specular reflectance of the surface at normal incidence ($0 \le F_0 \le 1$), and δ is the delta function, which yields an acceleration due to the SRP of

$$\boldsymbol{a}_{\mathrm{SRP}} = -\sum_{k=1}^{N_{\mathrm{facets}}} \frac{F_{\mathrm{sun}} A_k f_k (\hat{\boldsymbol{L}} \cdot \hat{\boldsymbol{N}}_k)_+}{m_{\mathrm{so}} c} \times \left[(1 - s_k (F_0)_k) \hat{\boldsymbol{L}} + \left(\frac{2}{3} d_k \rho_k + 2 s_k (F_0)_k \hat{\boldsymbol{L}} \cdot \hat{\boldsymbol{N}}_k \right) \hat{\boldsymbol{N}}_k \right] \quad (5)$$

where F_{sun} is the total solar flux over all wavelengths. This is the conventional formula typically used to calculate the SRP acceleration for a facet-based model (e.g., equivalent to equations derived in Appendix A in [8]).

For a more complicated BRDF, the exact solution obtained by numerically integrating Eq. (2) is different than the idealized solution obtained by Eq. (5). The numerical integration of Eq. (2) over the full hemisphere, however, is time consuming and might be prohibitive to calculate in certain applications. In this paper, correction factors for Eq. (5) are developed and the acceleration is calculated in a single step by using

$$\boldsymbol{a}_{\mathrm{SRP}} = -\sum_{k=1}^{N_{\mathrm{facets}}} \frac{F_{\mathrm{sun}} A_k f_k (\hat{\boldsymbol{L}} \cdot \hat{\boldsymbol{N}}_k)_+}{m_{\mathrm{SO}} c} \times \left[\begin{array}{l} (1 - (\Delta_{s1})_k s_k (F_0)_k) \hat{\boldsymbol{L}} \\ + \left(\frac{2}{3} (\Delta_d)_k d_k \rho_k + 2 (\Delta_{s2})_k s_k (F_0)_k \hat{\boldsymbol{L}} \cdot \hat{\boldsymbol{N}}_k \right) \hat{\boldsymbol{N}}_k \end{array} \right] \quad (6)$$

where the Δ factors depend on the illumination angle and possibly parameters within the BRDF model. Thus, for $\Delta_d = 1$, the diffuse reflectance is Lambertian and, for $\Delta_{s1} = \Delta_{s2} = 1$, the specular reflectance is mirror-like. The further these Δ factors are from unity, the greater the difference between the BRDF model and the idealized BRDF of Eq. (4). Without loss of generality, the same BRDF corrections can be applied when calculating the radiation pressure from a different illumination source, as with Earth–albedo/Earth–infrared radiation pressure (ERP). In addition, the BRDF reflectivity differences need to be accounted for when calculating the thermal radiation pressure (TRP) due to emission from the SO itself.

III. BRDF Descriptions

The BRDF reflectance model is an approximation of the true BRDF of the SO surfaces. There is no community-wide consensus, however, regarding which analytic BRDF model is best at representing different materials. A full comparison of various models to measurements of actual BRDFs is beyond the scope of this paper. Instead, the reflectance models of Ashikhmin and Shirley [9] and Cook and Torrance [10], are used in this paper to present a sampling of two very different BRDF models for comparison.

To be used as a prediction tool for brightness and radiation pressure calculations, an important aspect of a physically correct BRDF is energy conservation. The total diffuse and specular reflectivity can be calculated separately using

$$R_{\mathrm{diff}} = \int_0^{2\pi} \int_0^{\pi/2} dR_d \cos\theta_r \sin\theta_r \, \mathrm{d}\theta_r \, \mathrm{d}\phi_r \quad (7)$$

$$R_{\mathrm{spec}} = \int_0^{2\pi} \int_0^{\pi/2} sR_s \cos\theta_r \sin\theta_r \, \mathrm{d}\theta_r \, \mathrm{d}\phi_r \quad (8)$$

where, if energy is to be conserved, the total reflectivity must be less than or equal to unity:

$$R_{\mathrm{diff}} + R_{\mathrm{spec}} \leq 1 \quad (9)$$

For the BRDF given in Eq. (4), this corresponds to constant values of $R_{\mathrm{diff}} = d\rho$ and $R_{\mathrm{spec}} = sF_0$. The remaining energy not reflected by the surface is either transmitted or absorbed and, of the absorbed energy, some fraction can be thermally reemitted. In this paper, it is assumed the transmitted energy is zero and, thus, the absorptivity of the surface can be calculated by

$$\alpha_s = 1 - (R_{\mathrm{diff}} + R_{\mathrm{spec}}) \quad (10)$$

The absorbed energy, thermal energy transfer between contacting surfaces, and subsequent reemitted thermal energy is decoupled but accounted for in the new TRP model developed in Sec. V.

A. Ashikhmin–Shirley BRDF

Also known as the Anisotropic Phong BRDF, the diffuse and specular bidirectional reflectances are calculated using [9]

$$R_d = \frac{28\rho}{23\pi}(1 - sF_0)\left[1 - \left(1 - \frac{\hat{\boldsymbol{N}} \cdot \hat{\boldsymbol{L}}}{2}\right)^5\right]\left[1 - \left(1 - \frac{\hat{\boldsymbol{N}} \cdot \hat{\boldsymbol{V}}}{2}\right)^5\right] \quad (11)$$

$$R_s = \frac{\sqrt{(n_u + 1)(n_v + 1)}}{8\pi} \frac{F}{(\hat{\boldsymbol{V}} \cdot \hat{\boldsymbol{H}}) \max[\hat{\boldsymbol{N}} \cdot \hat{\boldsymbol{L}}, \hat{\boldsymbol{N}} \cdot \hat{\boldsymbol{V}}]} \times (\cos\alpha)^{n_u \cos^2\beta + n_v \sin^2\beta} \quad (12)$$

where Eq. (11) is a non-Lambertian diffuse BRDF, and the Fresnel reflectance F in Eq. (12) is given by Schlick's approximation [11]:

$$F = F_0 + \left(\frac{1}{s} - F_0\right)\left(1 - \hat{\boldsymbol{V}} \cdot \hat{\boldsymbol{H}}\right)^5 \quad (13)$$

In addition to d, ρ, and F_0, the Ashikhmin–Shirley BRDF has two exponential factors (n_u, n_v) that define the anisotropic reflectance properties of each surface (e.g., a preferential direction resulting from, say, brushed metal).

Figure 2 shows the dependence of R_{diff} and R_{spec} on illumination angle and exponential factor ($n = n_u = n_v$) for the Ashikhmin–Shirley BRDF where the integrals of Eqs. (7) and (8) are computed numerically. In both plots, $d = s = 0.5$ and, thus, the simple BRDF of Eq. (4) yields $R_{\mathrm{diff}} = R_{\mathrm{spec}} = 0.25$ and 0.495 for the left and right plots, respectively. The Ashikhmin–Shirley diffuse and specular reflectivities are not constant, however, but rather complicated functions of illumination angle, exponential factor, and the diffuse and specular reflectances. In all cases, however, $R_{\mathrm{diff}} + R_{\mathrm{spec}} \leq 1$; thus, energy is conserved.

B. Cook–Torrance BRDF

The diffuse and specular bidirectional reflectances are calculated using [10]

$$R_d = \rho/\pi \quad (14)$$

$$R_s = \frac{\mathrm{DGF}}{4(\hat{\boldsymbol{N}} \cdot \hat{\boldsymbol{L}})(\hat{\boldsymbol{N}} \cdot \hat{\boldsymbol{V}})} \quad (15)$$

where, again, Eq. (14) is the Lambertian diffuse BRDF, as in Eq. (4), and the facet slope distribution function D, the geometrical attenuation factor G, and the reflectance of a perfectly smooth surface F are given by

$$D = \frac{1}{\pi m^2 \cos^4\alpha} e^{-[\tan\alpha/m]^2} \quad (16)$$

$$G = \min\left\{1, \frac{2(\hat{\boldsymbol{N}} \cdot \hat{\boldsymbol{H}})(\hat{\boldsymbol{N}} \cdot \hat{\boldsymbol{V}})}{\hat{\boldsymbol{V}} \cdot \hat{\boldsymbol{H}}}, \frac{2(\hat{\boldsymbol{N}} \cdot \hat{\boldsymbol{H}})(\hat{\boldsymbol{N}} \cdot \hat{\boldsymbol{L}})}{\hat{\boldsymbol{V}} \cdot \hat{\boldsymbol{H}}}\right\} \quad (17)$$

$$F = \frac{(g - \hat{\boldsymbol{V}} \cdot \hat{\boldsymbol{H}})^2}{2(g + \hat{\boldsymbol{V}} \cdot \hat{\boldsymbol{H}})^2}\left\{1 + \frac{[\hat{\boldsymbol{V}} \cdot \hat{\boldsymbol{H}}(g + \hat{\boldsymbol{V}} \cdot \hat{\boldsymbol{H}}) - 1]^2}{[\hat{\boldsymbol{V}} \cdot \hat{\boldsymbol{H}}(g - \hat{\boldsymbol{V}} \cdot \hat{\boldsymbol{H}}) + 1]^2}\right\} \quad (18)$$

with $g^2 = n_{\mathrm{est}}^2 + (\hat{\boldsymbol{V}} \cdot \hat{\boldsymbol{H}})^2 - 1$ and the index of refraction

Downloaded by AFRL/DII on January 22, 2014 | http://arc.aiaa.org | DOI: 10.2514/1.60577

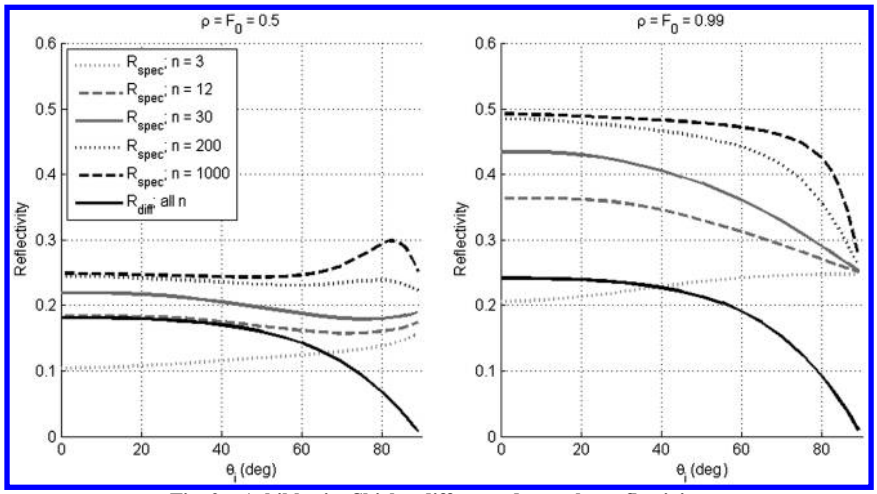

Fig. 2 Ashikhmin–Shirley diffuse and specular reflectivity.

$$n_{\text{est}} = \frac{1+\sqrt{F_0}}{1-\sqrt{F_0}}$$

In addition to d, ρ, and F_0, the Cook–Torrance BRDF has a facet slope m parameter that defines the reflectance properties of each surface. The facet slope parameter of the Cook–Torrance BRDF and the exponential factor of the Ashikhmin–Shirley BRDF are roughly related by $n = 2/m^2$.

Figure 3 shows the dependence of R_{diff} and R_{spec} on illumination angle and exponential factor for the Cook–Torrance BRDF where the integrals of Eqs. (7) and (8) are computed numerically and $d = s = 0.5$. Again, the simple BRDF of Eq. (4) yields $R_{\text{diff}} = R_{\text{spec}} = 0.25$ and 0.495 for the left and right plots, respectively, and so the deviations of the Cook–Torrance BRDF model from the simple BRDF are smaller. Specifically, the Lambertian diffuse portion is the same and produces a constant diffuse reflectivity. The specular portion becomes more mirror-like for smaller values of facet slope, although with differences in the reflectivity at high solar illumination angles. In all cases, energy is conserved.

In general, the parameters that comprise a BRDF model are wavelength dependent. For simplicity, this wavelength dependence is ignored and SRP correction factors for constant parameter values are derived. Accounting for the wavelength dependence would simply involve a sum of separate solutions weighted by the solar flux at that particular wavelength.

IV. Deriving the SRP Delta Factors

The diffuse component of the Cook–Torrance BRDF is Lambertian and, thus, the diffuse Δ factor is simply unity. The diffuse component of the Ashikhmin–Shirley BRDF is non-Lambertian, but the integral of Eq. (2) can be evaluated analytically. The resulting diffuse Δ factors are

$$\Delta_{d-\text{AS}}(\theta_i, sF_0) = \left[\frac{31}{32}(1-sF_0)\right]\left(\frac{1573}{1426}\right)\left[1-\left(1-\frac{\cos\theta_i}{2}\right)^5\right] \tag{19}$$

$$\Delta_{d-\text{CT}} = 1 \tag{20}$$

where the product of ρ and the term in the first square brackets in Eq. (19) is the equivalent Lambertian diffuse reflectance for the Ashikhmin–Shirley BRDF.

Values for the specular Δ factors can be numerically calculated at a particular illumination angle and set of BRDF parameters by comparing the numerical integration of the BRDF in Eq. (2),

$$\mathbf{L}' = \int_0^{2\pi}\int_0^{\pi/2} f_r(\hat{\boldsymbol{V}}\cdot\hat{\boldsymbol{N}},\lambda)\cos\theta_r\hat{V}\,\mathrm{d}\theta_r\,\mathrm{d}\phi_r \tag{21}$$

to the equivalent portion of Eq. (6) when only considering the specular component:

$$\mathbf{L}' = (1-\Delta_{s1}F_0)\hat{\boldsymbol{L}} + (2\Delta_{s2}F_0\hat{\boldsymbol{L}}\cdot\hat{\boldsymbol{N}})\hat{\boldsymbol{N}} \tag{22}$$

Specifically, for $\hat{\boldsymbol{L}} \neq \hat{\boldsymbol{N}}$,

$$\Delta_{s1}(p,\theta_i)_{\text{numerical}} = \frac{(\mathbf{L}'\cdot\hat{\boldsymbol{N}})\cos\theta_i - (\mathbf{L}'\cdot\hat{\boldsymbol{L}})}{F_0\sin^2\theta_i} \tag{23}$$

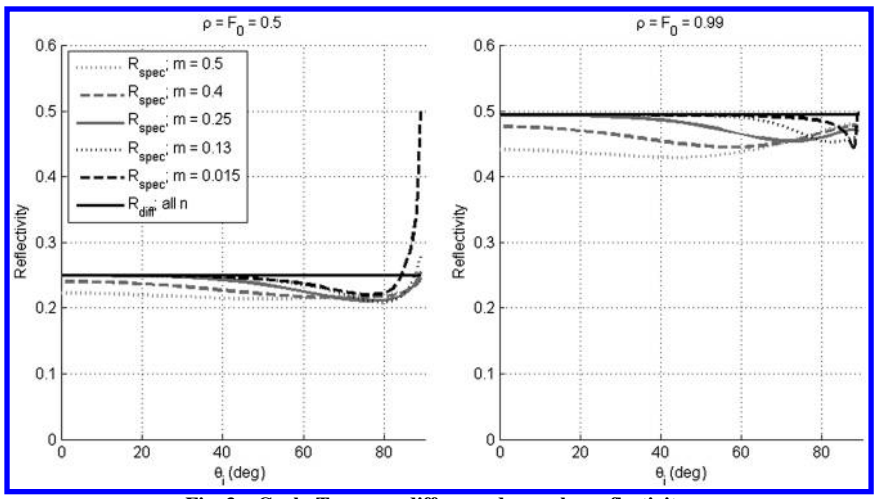

Fig. 3 Cook–Torrance diffuse and specular reflectivity.

Downloaded by AFRL/DII on January 22, 2014 | http://arc.aiaa.org | DOI: 10.2514/1.60577

$$\Delta_{s2}(p,\theta_i)_{\text{numerical}} = \frac{(\mathbf{L}'\cdot\hat{\boldsymbol{N}}) - (\mathbf{L}'\cdot\hat{\boldsymbol{L}})\cos\theta_i}{2F_0\cos\theta_i\sin^2\theta_i} \tag{24}$$

where p represents parameters within the BRDF model.

For $\hat{\boldsymbol{L}} = \hat{\boldsymbol{N}}$, the two values cannot be separated and only a composite value can be computed by

$$\frac{\mathbf{L}'\cdot\hat{\boldsymbol{N}}}{F_0} = -\Delta_{s1}(p,\theta_i)_{\text{numerical}} + 2\Delta_{s2}(p,\theta_i)_{\text{numerical}} \tag{25}$$

In this case, one of the specular Δ factors must be estimated using nonzero illumination angles as the illumination angle approaches zero, and the other can be calculated from Eq. (25).

Once a large number of these values is obtained for a variety of input values, either an empirical fit can be made or a lookup table can be constructed. For simplicity, the anisotropy of the Ashikhmin–Shirley BRDF model is suppressed by setting the two exponential factors equal to each other ($n_u = n_v = n$). To account for the anisotropy, a more complicated correction including an azimuthal dependence would be required. The two remaining Ashikhmin–Shirley parameters that are relevant to the Δ factors are the exponential factor n and the multiplication of the specular fraction with the specular reflectance at normal incidence sF_0. The microfacet slope m and the specular reflectance at normal incidence F_0 are relevant for the Cook–Torrance BRDF model. Consequently, much of the dependence on these parameters can be eliminated by first deriving analytic solutions at special limits. Thus, the specular Δ factors are derived in three steps. In the first two steps, the BRDF in certain limits is evaluated where an analytic solution in that limit can be calculated. These correspond to the limit of normal illumination ($\hat{\boldsymbol{L}} = \hat{\boldsymbol{N}}$) and the limit when the microfacet slope parameter goes to zero (for Cook–Torrance) or the exponential factor goes to infinity (for Ashikhmin–Shirley). The third step compares the numerical Δ factor values calculated for only the specular component to the analytic solution from the first two steps combined to determine the residual, and it is this residual that is turned into a lookup table.

A. Step One

In step 1, $\hat{\boldsymbol{L}} = \hat{\boldsymbol{N}}$. For the case of normal illumination, each BRDF can be simplified and the integral of Eq. (2) can be accomplished analytically. The resulting Δ factors are

$$\Delta_{s1-\text{AS}} = \Delta_{s2-\text{AS}} = \Delta_{\text{AS1}}(n) = 1 - \frac{2^{3-(n+1)/2} + 8(n+1)}{(n+5)(n+3)} \tag{26}$$

$$\Delta_{s1-\text{CT}} = \Delta_{s2-\text{CT}} = \Delta_{\text{CT1}}(m) = \left\{\begin{array}{l} \frac{2e^{1/m^2}}{m^2}\left[\text{Ei}\left(\frac{1}{m^2}\right) + \left(4+\frac{4}{m^2}\right)\text{Ei}\left(\frac{2}{m^2}\right) - \left(5+\frac{4}{m^2}\right)\text{Ei}\left(\frac{4}{3m^2}\right)\right] \\ +\left(3+\frac{6}{m^2}\right)e^{-1/3m^2} - \left(2+\frac{4}{m^2}\right)e^{-1/m^2} - 1 \end{array}\right\} \tag{27}$$

where Ei is the exponential integral function [12]. The derivation of Eqs. (26) and (27) are explained in more detail in the Appendix. Because of values approaching infinity, Eq. (27) is not calculable for small values of m and, therefore, an approximation must be used for $m < 0.045$ ($\Delta_{\text{CT1}}(m) = 1 - 0.0013m - 1.9634m^2$).

B. Step Two

In step 2, $m \to 0$ and $n \to \infty$. Again, as the microfacet slope approaches zero or the exponential factor approaches infinity, the BRDFs become more mirror-like and the integral of Eq. (2) can be accomplished. The resulting Δ factors are

$$\Delta_{s1-\text{AS}} = \Delta_{s2-\text{AS}} = \Delta_{\text{AS2}}(\theta_i, sF_0) = \frac{F(\theta_i, s, F_0)}{F_0} \tag{28}$$

$$\Delta_{s1-\text{CT}} = \Delta_{s2-\text{CT}} = \Delta_{\text{CT2}}(\theta_i, F_0) = \frac{F(\theta_i, F_0)}{F_0} \tag{29}$$

where F in Eq. (28) is Schlick's approximation of the Fresnel reflectance from Eq. (13), with $\hat{\boldsymbol{V}}\cdot\hat{\boldsymbol{H}} = \cos\theta_i$ in this limit, and F in Eq. (29) is the reflectance of a perfectly smooth surface defined in Eq. (18), again with $\hat{\boldsymbol{V}}\cdot\hat{\boldsymbol{H}} = \cos\theta_i$. The derivation is explained in more detail in the Appendix.

C. Step 3: Fitting the Residual

A total of 4488 separate values for each residual is calculated corresponding to 24 different values of illumination angle θ_i = [0, 2, 5, 10, 15, 20, 25, 30, 35, 40, 45, 50, 55, 60, 65, 70, 75, 80, 82, 84, 86, 87, 88, and 89 deg], 17 different values of microfacet slope m = [0.005, 0.01, 0.015, 0.02, 0.04, 0.06, 0.08, 0.1, 0.13, 0.16, 0.19, 0.22, 0.25, 0.3, 0.4, 0.5, 1] or exponential factor n = [1, 2, 3, 5, 7, 9, 12, 15, 20, 30, 50, 100, 200, 500, 1000, 5000, 10000], and 11 different values of specular reflectance at normal incidence F_0 = [0.01, 0.1, 0.2, 0.3, 0.4, 0.5, 0.6, 0.7, 0.8, 0.9, 0.99]. These values are chosen to have more measurements where the Δ factor residuals are changing the most rapidly (e.g., at grazing illumination angles).

The resulting data array is augmented into a $25\times19\times13$ array (corresponding to $\theta_i\times n\times F_0$) for Ashikhmin–Shirley, and a $25\times18\times13$ array (corresponding to $\theta_i\times m\times F_0$) for Cook–Torrance. Specifically, the $\theta_i = 89$ deg values are duplicated into a $\theta_i = 90$ deg matrix, an $m = 0$ or $n = 10^9$ value array is set to unity, the $n = 1$ values are duplicated into an $n = 0$ matrix, the $F_0 = 0.01$ values are duplicated into a $F_0 = 0$ matrix, and the $F_0 = 0.99$ values are duplicated into a $F_0 = 1$ matrix. Values for the residual functions δ_{s1} and δ_{s2} are extracted from the data arrays via sequential linear interpolations.

The final Δ factors are thus

$$\begin{aligned}\Delta_{s1-\text{AS}} &= \Delta_{\text{AS1}}(n)\Delta_{\text{AS2}}(\theta_i, sF_0)\delta_{s1-\text{AS}}(\theta_i, n, F_0)\\ \Delta_{s2-\text{AS}} &= \Delta_{\text{AS1}}(n)\Delta_{\text{AS2}}(\theta_i, sF_0)\delta_{s2-\text{AS}}(\theta_i, n, F_0)\end{aligned} \tag{30}$$

$$\begin{aligned}\Delta_{s1-\text{CT}} &= \Delta_{\text{CT1}}(m)\Delta_{\text{CT2}}(\theta_i, F_0)\delta_{s1-\text{CT}}(\theta_i, m, F_0)\\ \Delta_{s2-\text{CT}} &= \Delta_{\text{CT1}}(m)\Delta_{\text{CT2}}(\theta_i, F_0)\delta_{s2-\text{CT}}(\theta_i, m, F_0)\end{aligned} \tag{31}$$

where $\Delta_{\text{AS1}}(n)$ is defined in Eq. (26), $\Delta_{\text{AS2}}(\theta_i, n, F_0)$ is defined in Eq. (28), $\Delta_{\text{CT1}}(m)$ is defined in Eq. (27), and $\Delta_{\text{CT2}}(\theta_i, F_0))$ is defined in Eq. (29). The valid range for these equations is all illumination angles ($0 \le \theta_i \le 90$ deg), all specular reflectances at normal incidence ($0 \le F_0 \le 1$), and all microfacet slope values less than one ($0 \le m \le 1$) or exponential factors less than 10^9 ($0 \le n \le 10^9$).

Figures 4 and 5 show the progression from no correction through step 3 using the Δ factors described for the two BRDF models. These plots are the percentage difference with respect to the acceleration at normal incidence for values of illumination angle, microfacet slope or exponential factor, and specular reflectance at normal incidence. All values are midway between entries in the lookup tables, and so they represent the worst deviations that might occur. Note how, in both cases, step 1 corrects the accelerations exactly for normal illumination, as expected. In addition, step 2 improves the low slope values (Cook–Torrance) and high exponential factor values (Ashikhmin–Shirley), as expected. Note that in both figures, the y-axis scale in the step 3 plot is one-tenth that of other plots.

The maximum uncorrected difference for Ashikhmin–Shirley is approximately 39% (for $n = 6$, $F_0 = 0.05$, and $\theta_i = 1$ deg), whereas corrected values are <0.2%. The maximum uncorrected difference for Cook–Torrance is approximately 7% (for $m = 0.275$, $F_0 = 0.95$, and $\theta_i = 1$ deg), whereas corrected values are <0.2%.

Finally, to evaluate the computational time saved by employing the Δ factors in Eq. (6) instead of numerically integrating Eq. (2), a comparison using the same computer and code is conducted. A single numerical integration of Eq. (2) over the entire hemisphere with an angular resolution of 0.1 deg takes approximately 600 s whereas a thousand sequential evaluations of Eq. (6) are completed in under 4 s. Employing the Δ factors in Eq. (6), however, takes about 10 times longer than using the simplified Eq. (5) without the Δ factors.

Downloaded by AFRL/DII on January 22, 2014 | http://arc.aiaa.org | DOI: 10.2514/1.60577

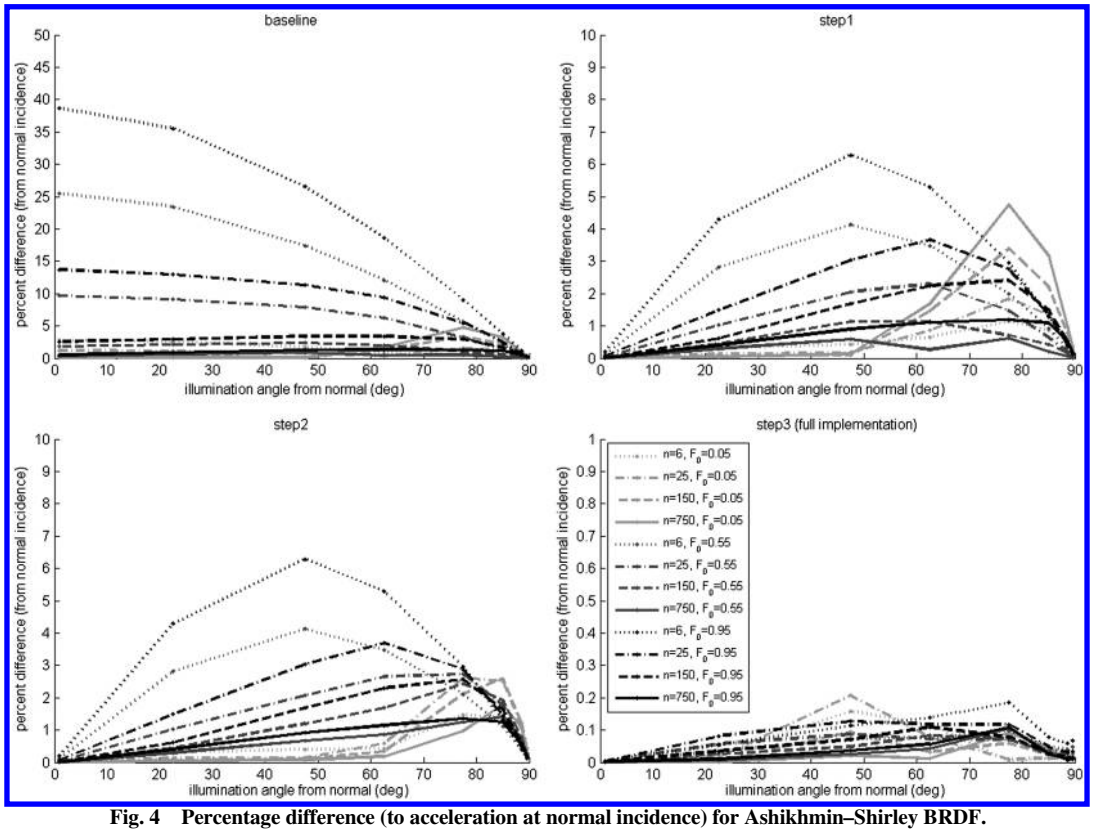

Fig. 4 Percentage difference (to acceleration at normal incidence) for Ashikhmin–Shirley BRDF.

V. Other Radiation Pressure Models

Other sources of radiation pressure exist where the difference from the baseline of Eq. (5) are comparable to the BRDF SRP correction of Eq. (6). Earth–albedo and Earth–infrared radiation pressure (ERP) is identical in form to the SRP where Earth's reflection in the visible and emission in the infrared takes the place of the sun as the illumination source. Calculation of the ERP acceleration is more complicated due to the larger solid angle subtended by Earth with respect to the SO and the introduction of an empirical model to represent Earth's albedo and emissivity. As with the SRP acceleration, the SO's surface BRDF also needs to be considered. The final radiation pressure to be considered is the SO's thermal radiation pressure (TRP). To calculate the TRP acceleration, the temperatures of the various surfaces of the SO must be known. This requires a model that calculates these temperatures

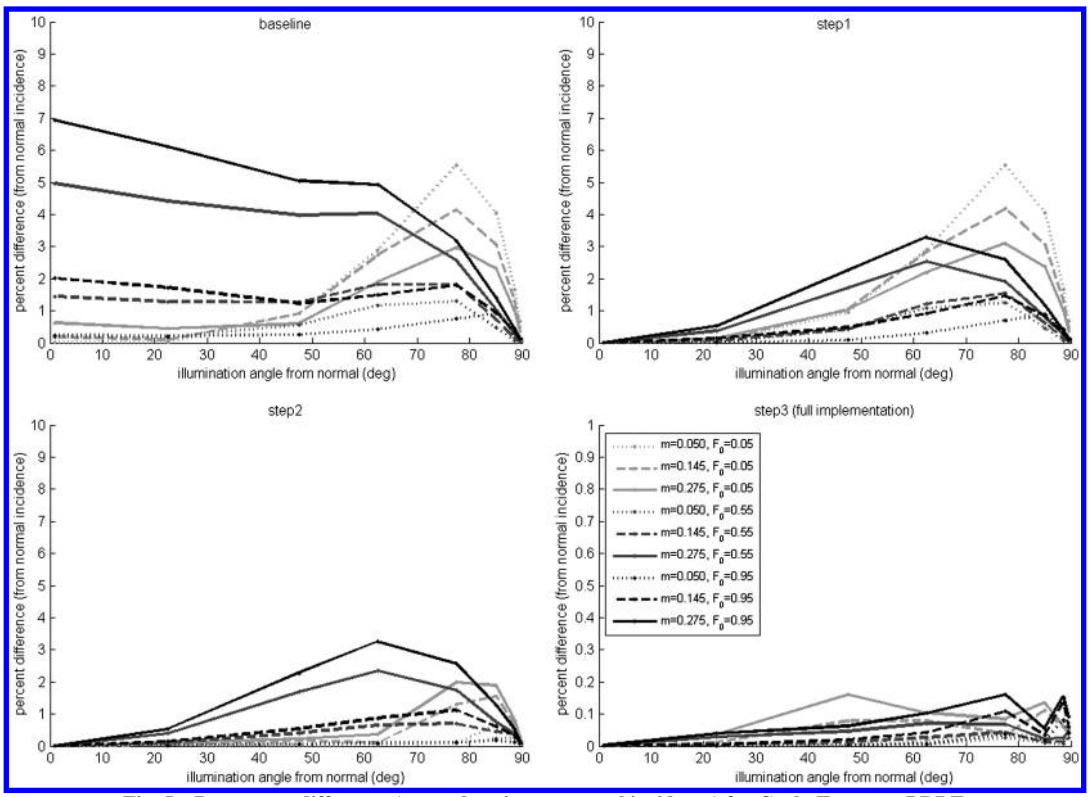

Fig. 5 Percentage difference (to acceleration at normal incidence) for Cook–Torrance BRDF.

Downloaded by AFRL/DII on January 22, 2014 | http://arc.aiaa.org | DOI: 10.2514/1.60577

given the SO's attitude, the passage of each surface into and out of shadow, and the thermal interconnection between surfaces.

A. Earth–Albedo/Earth–Infrared Radiation Pressure

A slightly modified model described in [13,14] is used to calculate the ERP acceleration. In this model, Earth is divided into N regions and Eq. (5) is used to calculate the contribution of each region to the SO's acceleration by using

$$\boldsymbol{a}_{\mathrm{ERP}} = -\sum_{k=1}^{N_{\mathrm{facets}}}\sum_{j=1}^{N}\frac{F_{\mathrm{Earth},j}A_k f_k(\hat{\boldsymbol{L}}_j\cdot\hat{\boldsymbol{N}}_k)_+}{m_{\mathrm{SO}}c} \times\left[(1-s_k(F_0)_k)\hat{\boldsymbol{L}}_j+\left(\frac{2}{3}d_k\rho_k+2s_k(F_0)_k\hat{\boldsymbol{L}}_j\cdot\hat{\boldsymbol{N}}_k\right)\hat{\boldsymbol{N}}_k\right] \tag{32}$$

The total Earth flux for each region j is calculated by

$$F_{\mathrm{Earth},j} = F_{\mathrm{sun}}\left[(a_E)_j(\cos\theta_j)_+ + \frac{1}{4}(\varepsilon_E)_j\right]\frac{4\pi R_\oplus^2}{N}\frac{(\cos\alpha_j)_+}{\pi r_j^2} \tag{33}$$

where F_{sun} is the total solar flux as used in Eq. (5), $(a_E)_j$ is Earth's albedo as calculated using an empirical model defined next, θ_j is the angle between the solar illumination vector and normal to the surface of the jth Earth region, $(\varepsilon_E)_j$ is Earth's emissivity as calculated using an empirical model defined next, $R_\oplus$ is Earth's radius, α_j is the angle between the viewing vector (center of jth Earth region to SO) and normal to the surface of the Earth region, and r_j is the distance from the center of jth Earth region to the SO. References [13,14] use $N = 19$ regions consisting of a single subobject region and 6 and 12 regions in two concentric rings, all with equal projected and attenuated areas. Instead, as reflected in Eq. (32), in this paper the entire Earth surface is divided into N evenly distributed and equal area regions, and ERP accelerations are calculated from only those regions visible from the SO ($\cos\alpha_j > 0$). The variable N is chosen based on the SO's altitude to ensure at least 40 regions are visible at any one time.

The process used to generate the N evenly distributed regions employs a slight variation to the prescription of [15,16]. Specifically, the region centers (latitude and longitude in radians) are calculated using

$$\lambda_j = \tan^{-1}\left(\frac{\sqrt{1-z_j^2}}{z_j}\right)-\frac{\pi}{2} \tag{34}$$

$$l_j = \mathrm{mod}(l_{j-1}+\pi(3-\sqrt{5}),2\pi) \tag{35}$$

for $j = 1\ldots N$, where $z_1 = 1-1/N$, $l_1 = 0$, and $z_j = z_{j-1}-2/N$. Figure 6 displays this distribution for $N = 100$ and $N = 400$ for Figs. 6a and 6b, respectively.

Earth's albedo and emissivity are empirical functions of latitude and also account for seasonal variations,

$$a_E = a_0 + a_1P_1(\sin\lambda) + a_2P_2(\sin\lambda) \tag{36}$$

$$\varepsilon_E = \varepsilon_0 + \varepsilon_1P_1(\sin\lambda) + \varepsilon_2P_2(\sin\lambda) \tag{37}$$

where $a_0 = 0.34$, $a_1 = 0.1\cos[2\pi(\mathrm{JD}-t_0)/365.25]$, $a_2 = 0.29$, $\varepsilon_0 = 0.68$, $\varepsilon_1 = -0.07\cos[2\pi(\mathrm{JD}-t_0)/365.25]$, and $\varepsilon_2 = -0.18$. JD is the Julian Date, $t_0 = 2444960.5$ (22 December 1981), λ is Earth region's latitude, and $P_1(x) = x$ and $P_2(x) = (3x^2-1)/2$ (Legendre polynomials of orders 1 and 2, respectively). Although computationally expensive, the equivalent to Eq. (6) can be easily used to calculate the BRDF corrected ERP:

$$\boldsymbol{a}_{\mathrm{ERP}} = -\sum_{k=1}^{N_{\mathrm{facets}}}\sum_{j=1}^{N}\frac{F_{\mathrm{Earth},j}A_k f_k(\hat{\boldsymbol{L}}_j\cdot\hat{\boldsymbol{N}}_k)_+}{m_{\mathrm{SO}}c} \times\left[\begin{array}{l}(1-(\Delta_{s1})_{j,k}s_k(F_0)_k)\hat{\boldsymbol{L}}_j+\\ \left(\frac{2}{3}(\Delta_d)_{j,k}d_k\rho_k+2(\Delta_{s2})_{j,k}s_k(F_0)_k\hat{\boldsymbol{L}}_j\cdot\hat{\boldsymbol{N}}_k\right)\hat{\boldsymbol{N}}_k\end{array}\right] \tag{38}$$

B. Thermal Radiation Pressure

A new thermal model is developed that is compatible with the surface BRDF. First, however, the thermal model of [17] is examined to provide a comparison in calculating the TRP. In this model, as with the SRP and ERP, the contribution of each facet is calculated separately and then summed. The acceleration is

$$\boldsymbol{a}_{\mathrm{TRP}} = -\sum_{k=1}^{N_{\mathrm{facets}}}\frac{2\varepsilon_k\sigma T_k^4A_k}{3m_{\mathrm{SO}}c}\hat{\boldsymbol{N}}_k \tag{39}$$

where ε_k is the emissivity of the particular surface, σ is the Stefan–Boltzmann constant, and T_k is the temperature of the particular surface. This equation assumes the emissivity is independent of emission angle (i.e., it can be represented by a Lambertian-like function). The temperatures are determined using empirical functions of the form

$$T = k_1 + k_2\cos\left(\frac{\theta_i}{k_3}\right)\left[1-\exp\left(\frac{-(t_1+s_1)}{k_4}\right)\right] \tag{40}$$

where

$$s_1 = -k_4\ln\left\{\max\left[1-\exp\left(\frac{-t_2}{k_5}\right)\frac{\cos\theta_{\mathrm{shadow}}}{\cos\theta_{\mathrm{sun}}},0.0001\right]\right\} \tag{41}$$

for illuminated surfaces, and

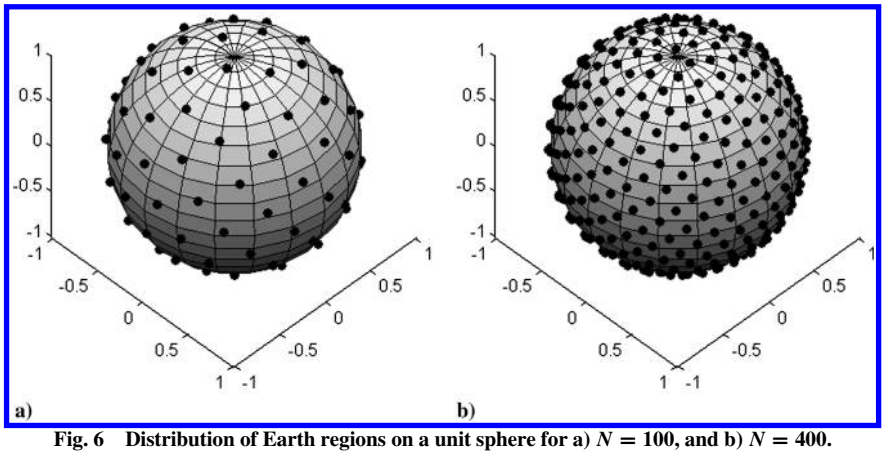

Fig. 6 Distribution of Earth regions on a unit sphere for a) $N = 100$, and b) $N = 400$.

Downloaded by AFRL/DII on January 22, 2014 | http://arc.aiaa.org | DOI: 10.2514/1.60577

$$T = k_1 + k_2 \exp\left[\frac{-(t_2 + s_2)}{k_5}\right] \tag{42}$$

where

$$s_2 = -k_5 \ln\left\{\max\left[\cos\left(\frac{\theta_{\text{shadow}}}{k_3}\right), 0.0001\right]\right\} \tag{43}$$

for surfaces in shadow where the temperature cools to some specified minimum in a time dependent on the material characteristics. The small value of 0.0001 in Eqs. (41) and (43) is added to keep the functions from becoming infinite. The adjustable material parameters for each surface are k_1 (cold equilibrium temperature), k_2 (difference between cold and hot equilibrium temperatures), k_3 (rotational rate/thermal inertia constant), k_4 (transition time from hot to cold equilibrium temperature), and k_5 (transition time from cold to hot equilibrium temperature). The other quantities are values that need to be calculated for a particular surface: t_1 (time since shadow exit), t_2 (time since shadow entry), θ_i (illumination angle), θ_{shadow} (illumination angle at shadow entry), and θ_{sun} (illumination angle at shadow exit).

Implicit in this model is the emissivity as related to the diffuse and specular reflectances. For the simple Lambertian diffuse and mirror-like specular BRDF with no wavelength dependence (so the emissivity equals the absorptivity), to conserve energy, this reduces to a value identical to Eq. (10):

$$\varepsilon = \alpha_s = 1 - R_{\text{diff}} - R_{\text{spec}} = 1 - d\rho - sF_0 \tag{44}$$

Empirical values for various surfaces of the TOPEX/Poseidon spacecraft, as modeled in [17], are shown in columns 1–8 in Table 1 (from Table 5 in [17]). The values to be modeled in this simulation are representative of these values and are shown in column 9.

The new TRP model that is physically consistent with the BRDF again uses Eq. (39) to calculate the acceleration. The difference is in how the emissivity and temperature of each surface of the SO are calculated. The temperature of a surface depends on three quantities: 1) heating of the surface due to radiation (e.g., solar or Earthshine), 2) cooling of the surface due to radiation (e.g., emission that produces the TRP), and 3) heating/cooling of the surface due to conduction (e.g., connection to other surfaces or components of the SO). From one time step to the next, this can be summarized in the equation

$$(T_{i+1})_k = (T_i)_k + \frac{(P_{\text{absorb}} + P_{\text{emit}} + P_{\text{conduct}})_k \Delta t}{C_k} \tag{45}$$

where C is the heat capacity related to the surface (in joules per kelvin). The power being absorbed by the surface can be represented by

$$(P_{\text{absorb}})_k = \sum_{j=1}^{N_{\text{sources}}} (\alpha_s)_{j,k} F_j A_k (\hat{\boldsymbol{L}}_j \cdot \hat{\boldsymbol{N}}_k)_+ \tag{46}$$

where F_j is the total flux over all wavelengths of an illumination source (e.g., sun or Earth region), A is the surface area, $\hat{\boldsymbol{L}}_j$ is the direction to the illumination source, $\hat{\boldsymbol{N}}$ is the surface normal, and the absorptivity is given by

$$(\alpha_s)_{j,k} = 1 - (R_{\text{diff}})_{j,k} - (R_{\text{spec}})_{j,k} \tag{47}$$

Table 1 Sample TRP model values

	1	2	3	4	5	6	7	8	9
k_1, K	181	168	191	190	240	103	236	234	250
k_2, K	233	178	18	63	98.5	125	110	96	50
k_3	1.25	1.00	1.05	1.00	1.06	1.15	1.00	1.00	1.25
k_4, s	621	282	759	426	519	680	805	806	700
k_5, s	111	120	624	487	767	413	828	866	500

To be consistent with the BRDF, R_{diff} and R_{spec} must be calculated using Eqs. (7) and (8) for the particular illumination conditions and BRDF model parameters. In practice, R_{diff} can be calculated analytically for the BRDF models detailed in this paper whereas a lookup table similar to the Δ factors in SRP modeling can be constructed for R_{spec}. This is done using the same data array as specified in Sec. IV for the Δ factors. Note that P_{absorb} is always positive. The power being emitted from the surface can be represented by

$$(P_{\text{emit}})_k = -\varepsilon_k A_k \sigma T_k^4 \tag{48}$$

which is simply the emitted radiation at a particular temperature. The emissivity of the kth facet to be used in Eqs. (39) and (48), to be consistent with the surface BRDF, is calculated using

$$\varepsilon_k = 1 - (R_{\text{diff}})_{\hat{\boldsymbol{L}}=\hat{\boldsymbol{N}}} - (R_{\text{spec}})_{\hat{\boldsymbol{L}}=\hat{\boldsymbol{N}}} \tag{49}$$

where the $\hat{\boldsymbol{L}} = \hat{\boldsymbol{N}}$ notation in the subscript signifies these are the diffuse and specular reflectivity associated with that geometry for the given BRDF parameters. Again, Eqs. (7) and (8) are used to calculate R_{diff} and R_{spec} and, in practice, R_{diff} is calculated analytically and a lookup table is used to determine R_{spec}. Note that P_{emit} is always negative. Finally, the power being conducted to or from the surface can be represented by

$$(P_{\text{conduct}})_k = \sum_{kk=1}^{N_{\text{body}}} A_{kk,k} k_{kk,k} (\nabla T)_{kk,k} \tag{50}$$

where k, A, and (∇T) are the various conductivities, contact surface areas, and temperature gradients between the k surface and the other surfaces of the object. P_{conduct} is positive when energy flows into the surface and negative when energy flows out of the surface.

The additional parameters required for each surface in this model beyond those associated with the BRDF involve a term related to the surface heat capacity, in Eq. (45), and terms related to the conductivities and contact surface areas between the surface and other parts of the object, in Eq. (50). In practice, the assumption that Eq. (50) and the associated parameters can be replaced by two parameters is made such that

$$(P_{\text{conduct}})_k = -K_k (T_k - T_{\text{body}}) \tag{51}$$

where K is a term related to conductivity of each surface (in watts per kelvin) and T_{body} is an equilibrium temperature for the body as a whole. Thus, for a cube, this TRP model requires 13 total parameters to represent the SO as opposed to 30 total parameters in the model in [17]. When all the surfaces are identical, three total parameters are necessary as opposed to five total parameters in the model in [17].

The temperatures of all six sides of a slowly rotating cube fixed in space with the sun as the only illumination source as predicted by the model in [17] using the values in column 9 of Table 1 are calculated and displayed in Fig. 7. The cube is rotating at 0.017 rad/s about its z axis. The slight discontinuity on the declining slope of the $\pm x$ and $\pm y$ temperature curves corresponds to the time when the side goes into shadow due to the rotation of the cube, and the temperature changes from being calculated with Eqs. (40) and (41) to Eqs. (42) and (43).

The $-z$ axis of the cube is facing away from the sun, and so is at the constant cold temperature of $k_1 = 250$ K, whereas the $+z$ axis of the cube is illuminated by the sun at a constant nonnormal angle, and so is at a constant temperature less than $k_1 + k_2 = 300$ K. The other sides alternatively are illuminated by the sun and then are in shadow and, because they are identical, they exhibit the same temperature profile as a function of time.

Figure 8 displays the temperatures of all six sides of the same cube using the new TRP BRDF corrected model with $C = 9000$ J/K, $K = 20$ W/K, and $T_{\text{body}} = 258$ K, and the Ashikhmin–Shirley BRDF with $\rho = F_0 = 0.5$, $d = s = 0.5$, and $n_u = n_v = 10$. The TRP model values are determined by trial and error to produce temperature profiles similar to those in Fig. 7. In general, adjusting C

Downloaded by AFRL/DII on January 22, 2014 | http://arc.aiaa.org | DOI: 10.2514/1.60577

Downloaded by AFRL/DII on January 22, 2014 | http://arc.aiaa.org | DOI: 10.2514/1.60577

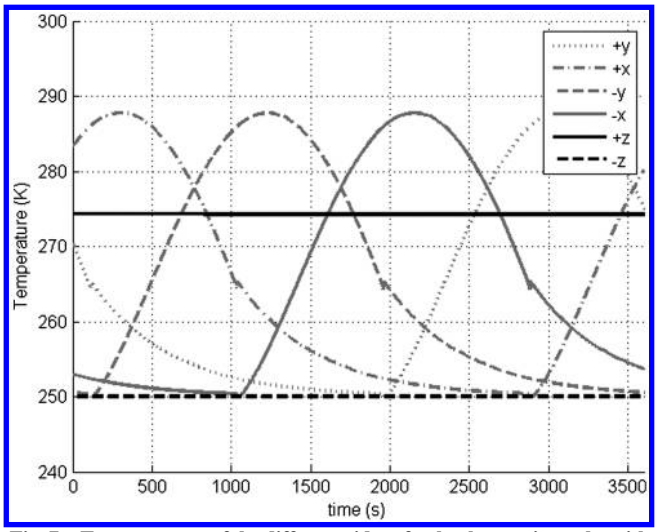

Fig. 7 Temperatures of the different sides of a slowly rotating cube with identical Marshall–Luthke surface parameters.

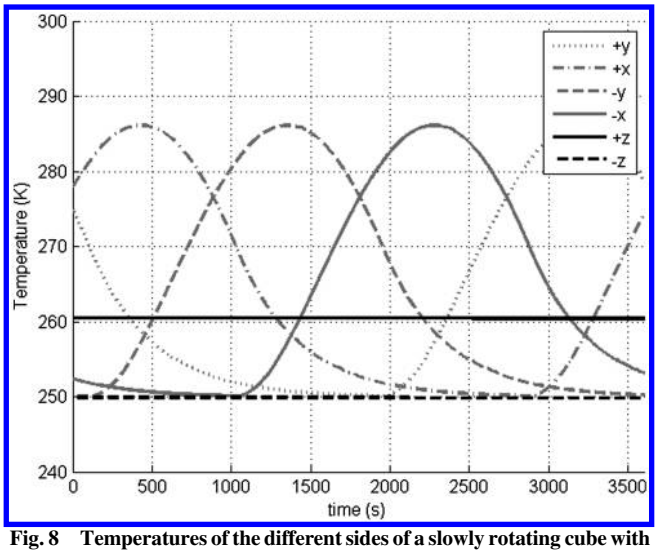

Fig. 8 Temperatures of the different sides of a slowly rotating cube with identical surface parameters of new TRP model.

alters the rate at which the surface heats and cools, with a greater value of C resulting in a longer heating/cooling time, adjusting K alters the peak temperature, with a greater value of K resulting in a lower peak temperature, and adjusting T_{body} alters the overall level of the temperature profile.

There are some features between the models that are not reconciled. Most notable is the temperature of the $+z$ side (surface normal along $+z$ body axis). In both models, it is constant due to the constant solar illumination. The level in the model in [17], however, is significantly higher than the new model. The other significant difference is the timing of the peak temperature on the x-axis and y-axis sides with the model in [17] peaking earlier than the new model. It is likely that the new model is unable to replicate exactly the temperature profiles of the model in [17]. The new model, however, has the advantage of being physics based and reconciled with the surface BRDF, and so is used in the remainder of the paper.

VI. Orbit and Attitude Propagation

The principal purpose of the trajectory and attitude modeling carried out in this paper is to emphasize the difference in behavior of the SO predicted by conventional surface force models with that predicted by BRDF-corrected techniques. Hence, the conservative force field is treated simplistically whereas the surface forces are given a rigorous formulation.

In this paper, the position and velocity of an Earth orbiting SO are denoted by $\boldsymbol{r}^I = [x, y, z]^I$ and $\boldsymbol{v}^I = [v_x, v_y, v_z]^I$, respectively. The Newtonian two-body gravitational equations of motion with radiation pressure acceleration in Earth-centered inertial coordinates are given by

$$\ddot{\boldsymbol{r}}^I = -\frac{\mu}{\|\boldsymbol{r}^I\|^3}\boldsymbol{r}^I + \boldsymbol{a}^I_{\text{total}} + \boldsymbol{a}^I_{J2} \tag{52}$$

where the term μ represents the gravitational parameter of Earth and $\boldsymbol{a}^I_{\text{total}} = \sum_{k=1}^{N_{\text{facets}}} \boldsymbol{a}^I_k$ represents the acceleration perturbation due to the various radiation pressures as described earlier and summed over all the surfaces, whereas $\boldsymbol{a}^I_{J2}$ is the gravitational perturbation due to nonsymmetric distribution of mass along the lines of latitude of Earth [18]. A number of parameterizations exists to specify attitude, including Euler angles, quaternions, and Rodrigues parameters. This paper uses the quaternion [19].

The angular velocity dynamic equation can be written as

$$\dot{\boldsymbol{\omega}} = \bar{\bar{J}}^{-1}(M - [\boldsymbol{\omega}\times]\bar{\bar{J}}\boldsymbol{\omega}) \tag{53}$$

where $\bar{\bar{J}}$ is the inertia tensor for the SO, $\boldsymbol{M}$ are any external applied torques, and ω is the angular velocity. The SO is assumed to be a rectangular prism (sides a and b and length l); therefore, the principal components of the inertia tensor are given by simple equations:

$$J_x = m_{\text{SO}}\frac{(a^2+b^2)}{12} \quad J_y = m_{\text{SO}}\frac{(a^2+l^2)}{12} \quad J_z = m_{\text{SO}}\frac{(l^2+b^2)}{12} \tag{54}$$

The radiation pressure moments can be calculated by considering that the forces act through the center of each facet. Then, the radiation pressure moment can be written as

$$\boldsymbol{M} = m_{\text{SO}}\sum_{k=1}^{N_{\text{facets}}}[\boldsymbol{r}^B_k\times]A(\boldsymbol{q})\boldsymbol{a}^I_k \tag{55}$$

where $\boldsymbol{r}^B_k$ is the location of the geometric center of each facet with respect to the center of mass of the SO in body coordinates and $A(\boldsymbol{q})$ is the attitude matrix calculated by the quaternion $\boldsymbol{q}$. The radiation pressure moment is used with Eq. (53) to simulate the rotational dynamics of the SO.

VII. Radiation Pressure Perturbation Comparisons

A 1 m cube ($a = b = l = 1$ m) HAMR object that is 1 kg in mass is placed in GEO and a 1000 km height sun-synchronous LEO orbit, with Table 2 listing the orbital details.

The orbit and attitude are propagated with five different radiation pressure combinations: 1) simplified SRP in Eq. (5), 2) BRDF-corrected SRP using the Ashikhmin–Shirley BRDF with $n_u = n_v = 10$ in Eq. (6), 3) BRDF-corrected SRP using the Cook–Torrance BRDF with $m = 0.45$ in Eq. (6), 4) simplified SRP in Eq. (5) and simplified ERP in Eq. (32), and 5) simplified SRP in Eq. (5) and new TRP model with $C = 9000$ J/K, $K = 20$ W/K, and $T_{\text{body}} = 258$ K using the Ashikhmin–Shirley BRDF with $n_u = n_v = 10$ in Eq. (39). The acceleration magnitudes are compared as well as the differences in total, radial, in-track, and cross-track distances as a function of

Table 2 Orbit specifications

	GEO	LEO
A, km	42,164	7378
e	0	0
i, deg	0	98
M_0, deg	90	90
Ω, deg	0	0
ω, deg	0	0

time. Each surface of the cube is identical with $\rho = F_0 = 0.5$ and $d = s = 0.5$.

In this simulation, the initial attitude, using the quaternion parameterization, is set to $\boldsymbol{q} = [0.7041; 0.0199; 0.0896; 0.7041]^T$, the initial angular rate is zero, and the values are propagated for seven days with a 6 s time step. The initial date and time are 15 March 2010, 0400 hrs. It should be noted that these tests are designed to highlight the differing trajectory and attitude behaviors predicted by the various radiation pressures (SRP vs ERP vs TRP) and the two modeling approaches (traditional SRP vs BRDF-corrected SRP).

Figures 9 and 10 plot the absolute magnitude of the various radiation forces as a function of time for the HAMR object at GEO and LEO, respectively, for the last half-day of the simulation. Also plotted are the fractional differences of the BRDF-corrected SRP to the simplified SRP ($|\boldsymbol{a}_{\mathrm{SRP-AS}} - \boldsymbol{a}_{\mathrm{SRP}}|/|\boldsymbol{a}_{\mathrm{SRP}}|$ and $|\boldsymbol{a}_{\mathrm{SRP-CT}} - \boldsymbol{a}_{\mathrm{SRP}}|/|\boldsymbol{a}_{\mathrm{SRP}}|$) and the relative difference of the ERP and TRP to the simplified SRP ($|\boldsymbol{a}_{\mathrm{ERP}}|/|\boldsymbol{a}_{\mathrm{SRP}}|$ and $|\boldsymbol{a}_{\mathrm{TRP}}|/|\boldsymbol{a}_{\mathrm{SRP}}|$) for times when the object is out of eclipse. Whereas the relative magnitude of the TRP and difference of the BRDF-corrected SRP to the SRP remains about the same for each orbit type, the magnitude of the ERP depends on radial distance, as expected. Note the regular entry into and exit out of Earth eclipse in the acceleration time histories coincident with the orbit of the satellite.

Of particular note is the variation in magnitude of the BRDF-corrected SRPs to the others. This results from the fact that only the BRDF-corrected SRPs produce a torque on the HAMR object resulting in attitude changes and thus variations in the projected area and resulting acceleration. For a rectangular prism, $\boldsymbol{r}_k^B A(\boldsymbol{q})$ in Eq. (55) is proportional to $\hat{\boldsymbol{N}}_k$ for each surface. When combined with the simplified SRP in Eq. (5) with all the surfaces having the same reflectance properties, this reduces to the torque being proportional to

$$\boldsymbol{M} \propto \sum_{k=1}^{N_{\mathrm{facets}}} (\hat{\boldsymbol{L}} \cdot \hat{\boldsymbol{N}}_k)_+ (\hat{\boldsymbol{L}} \times \hat{\boldsymbol{N}}_k) \tag{56}$$

Because the surface normals of adjacent sides of a rectangular prism are orthogonal, this summation is zero for any vector $\hat{\boldsymbol{L}}$. Thus, for the SRP and ERP (with the simple Lambertian diffuse and mirror-like specular BRDF), the torque is always zero. For the TRP, the acceleration due to each surface is along the surface normal per Eq. (39), and so, when combined with Eq. (55), is also always zero for a rectangular prism. When combining Eq. (55) with the BRDF-corrected SRP in Eq. (6), however, the torque is now proportional to

$$\boldsymbol{M} \propto \sum_{k=1}^{N_{\mathrm{facets}}} [1 - sF_0(\Delta_{s1})_k](\hat{\boldsymbol{L}} \cdot \hat{\boldsymbol{N}}_k)_+ (\hat{\boldsymbol{L}} \times \hat{\boldsymbol{N}}_k) \tag{57}$$

The introduction of the Δ factor, which depends also on illumination angle and could be different for each surface, results in a net torque. This difference between the rotational dynamics of the SO when using the simplistic SRP of Eq. (5) and the BRDF-corrected SRP of Eq. (6), highlighted by the discovery of a hitherto unmodeled torque caused by the specular reflectance of the SO's surface, underscores the reason for this work as motivated in the introduction of this paper.

Figures 11 and 12 plot the total difference, radial difference, in-track difference, and cross-track difference for positions calculated using the BRDF-corrected SRP (both Ashikhmin–Shirley and Cook–Torrance), simplified SRP + ERP, and simplified SRP + TRP as compared to the position with simplified SRP only as a function of time for the last half-day of the simulation. In this particular simulation, the two BRDF-corrected SRPs show the largest variation

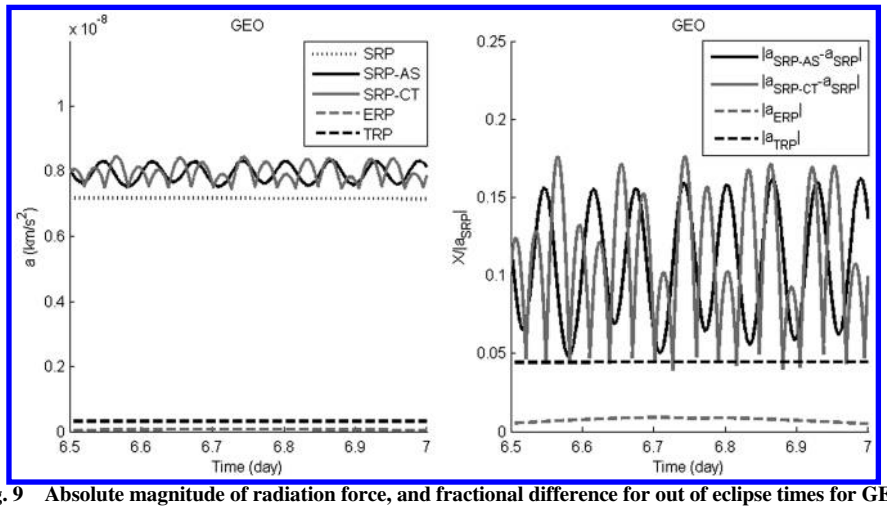

Fig. 9 Absolute magnitude of radiation force, and fractional difference for out of eclipse times for GEO.

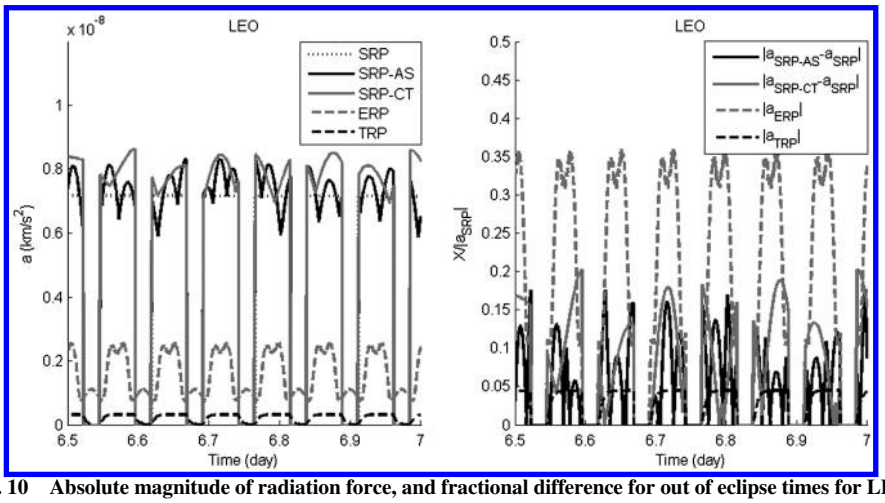

Fig. 10 Absolute magnitude of radiation force, and fractional difference for out of eclipse times for LEO.

Downloaded by AFRL/DII on January 22, 2014 | http://arc.aiaa.org | DOI: 10.2514/1.60577

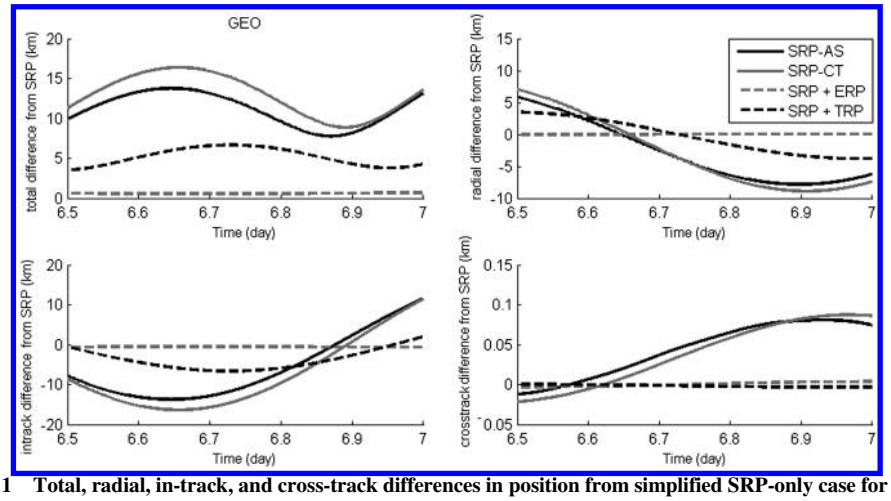

Fig. 11 Total, radial, in-track, and cross-track differences in position from simplified SRP-only case for GEO.

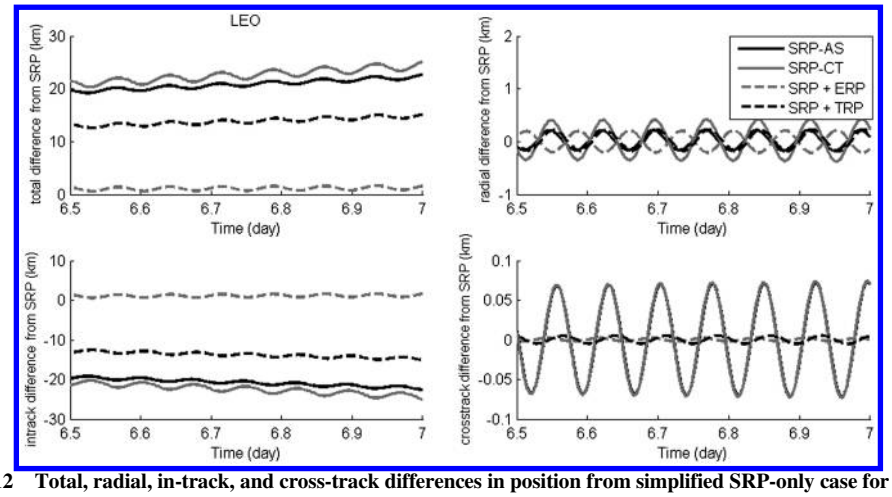

Fig. 12 Total, radial, in-track, and cross-track differences in position from simplified SRP-only case for LEO.

Downloaded by AFRL/DII on January 22, 2014 | http://arc.aiaa.org | DOI: 10.2514/1.60577

followed by the TRP and then the ERP with only minor differences. Variations in orbit, SO shape, and surface properties would undoubtedly produce different magnitudes. For high-fidelity orbit propagation, all these nongravitational forces need to be accounted for. In addition, the fact that the BRDF-corrected SRPs are similar, although not identical, is encouraging but highlights the need for further research regarding which BRDF model is the closest representation of the true BRDF of SO surfaces.

VIII. Conclusions

Brightness models are dependent on the surface bidirectional reflectance distribution function (BRDF). Current radiation pressure models, however, ignore the BRDF, even though the BRDF has a significant effect on the magnitude and direction of the resulting radiation pressures. The BRDF-induced perturbations in the solar radiation pressure (SRP) are significant enough to affect both tracking signatures and the ability to predict the orbital and attitudinal evolution of a space object (SO). The SRP, as well as the Earth–albedo/Earth–infrared radiation pressure and the thermal radiation pressure can be made physically consistent with the BRDF. For these results to be fully used, however, additional analyses regarding which analytic BRDF model best matches the true BRDF of the SO surfaces are needed.

Appendix A:

In the step 1 derivations of Sec. IV with $s = 1$ and $\hat{\boldsymbol{L}} = \hat{\boldsymbol{N}}$, the integral of Eq. (2) for a single facet reduces to

$$(\boldsymbol{a}_{\mathrm{SRP}})_{\hat{L}=\hat{N}} = \frac{(\boldsymbol{a}_{\mathrm{SRP}})^{\mathrm{mirror}}_{\hat{L}=\hat{N}}}{1+F_0}\left(1+\int_0^{2\pi}\int_0^{\pi/2} f_r \cos^2\theta_r \sin\theta_r \,\mathrm{d}\theta_r\,\mathrm{d}\phi_r\right) \tag{A1}$$

and Eq. (6) reduces to

$$(\boldsymbol{a}_{\mathrm{SRP}})_{\hat{L}=\hat{N}} = \frac{(\boldsymbol{a}_{\mathrm{SRP}})^{\mathrm{mirror}}_{\hat{L}=\hat{N}}}{1+F_0}[1+(2\Delta_{s2}-\Delta_{s1})F_0] \tag{A2}$$

where

$$(\boldsymbol{a}_{\mathrm{SRP}})^{\mathrm{mirror}}_{\hat{L}=\hat{N}} = -\frac{F_{\mathrm{sun}}Af}{m_{\mathrm{SO}}c}(1+F_0)\hat{\boldsymbol{N}} \tag{A3}$$

from Eq. (5). Note that $\hat{\boldsymbol{V}}\cdot\hat{\boldsymbol{N}} = \cos\theta_r$ has been used in Eq. (A1). Combining Eq. (A1) and Eq. (A2) and setting $\Delta = \Delta_{s1} = \Delta_{s2}$ yields

$$\Delta = \frac{1}{F_0}\int_0^{2\pi}\int_0^{\pi/2} f_r \cos^2\theta_r \,\sin\theta_r\,\mathrm{d}\theta_r\,\mathrm{d}\phi_r \tag{A4}$$

In the same limits, the Ashikhmin–Shirley BRDF in Eqs. (12) and (13) and Cook–Torrance BRDF in Eqs. (15–18) reduce to

$$f_r(\alpha) = \frac{F_0(n+1)}{8\pi}\cos^{n-1}\alpha \tag{A5}$$

$$f_r(\alpha) = \begin{pmatrix} \dfrac{F_0 e^{-[\tan \alpha/m]^2}}{4\pi m^2 \cos^4 \alpha \cos(2\alpha)} & \alpha < 30^o \\ \dfrac{F_0 e^{-[\tan \alpha/m]^2}}{2\pi m^2 \cos^4 \alpha} & \alpha > 30^o \end{pmatrix} \tag{A6}$$

In this geometry, there is a simple relation between the normal angle of the observer θ_r and the normal angle of the bisector between the illumination and observer α, namely $\alpha = \theta_r/2$, and there is no azimuthal dependence. As a result, the integral of Eq. (A4) can be done analytically in both cases to compute Δ. The resulting factors are given in Eqs. (26) and (27).

In the step 2 derivations of Sec. IV, with $s = 1$ and $n \to \infty$ (Ashikhmin–Shirley) or $m \to 0$ (Cook–Torrance), the Ashikhmin–Shirley and Cook–Torrance BRDFs reduce to the same function, given by

$$f_r = \frac{F\delta(\hat{\boldsymbol{V}} - \hat{\boldsymbol{R}})}{\cos \theta_i} \tag{A7}$$

which is nearly identical to the specular portion of the mirror-like term of Eq. (4) except that F_0 is replaced by F. For the Ashikhmin–Shirley BRDF, this is Schlick's approximation, which is given by Eq. (13), whereas for the Cook–Torrance BRDF, this is the Fresnel reflection from a perfectly smooth surface assuming the absorption coefficient is zero, which is given by Eq. (18). As with the simplified BRDF of Eq. (4), the integral of Eq. (2) can be done analytically in both cases and compared to Eq. (6) to compute Δ. The resulting factors are given in Eqs. (28) and (29).

Acknowledgements

This work is sponsored by a Small Business Innovative Research (SBIR) contract FA9453-11-C-0154 by the U.S. Air Force Research Laboratory at Kirtland Air Force Base, and contract FA8655-11-1-3043 by the European Office of Aerospace Research and Development, London, UK. The authors also wish to acknowledge useful discussions and technical contributions made by other members of the SBIR team: Daron Nishimoto, Keric Hill, Steve Lyke, Kris Hamada, and Channing Chow of Pacific Defense Solutions, LLC.

References

[1] Schildknecht, T., Musci, R., Flury, W., Kuusela, J., de Leon, J., and De Fatima Dominguez Palmero, L., "Properties of the High Area-to-Mass Ratio Space Debris Population in GEO," *The Advanced Maui Optical and Space Surveillance Technologies Conference*, Wailea, Maui, HI, Sept. 2005, pp. 216–223.

[2] Kelecy, T., Payne, T., Thurston, R., and Stansbery, G., "Solar Radiation Pressure Estimation and Analysis of a GEO Class of High Area-to-Mass Ratio Debris Objects," *AAS Astrodynamics Specialist Conference*, Vol. 129, Mackinac Island, MI, Paper 07-391, Aug. 2007, pp. 2205–2221;

[3] Kelecy, T., Baker, E., Seitzer, P., Payne, T., and Thurston, R., "Prediction and Tracking Analysis of a Class of High Area-to-Mass Ratio Debris Objects in Geosynchronous Orbit," *The Advanced Maui Optical and Space Surveillance Technologies Conference*, Wailea, Maui, HI, Sept. 2008, p. 33.

[4] Kelecy, T., and Jah, M., "Analysis of Orbit Prediction Sensitivity to Thermal Emissions Acceleration Modeling for High Area-to-Mass Ratio (HAMR) Objects," *The Advanced Maui Optical and Space Surveillance Technologies Conference*, Wailea, Maui, HI, Sept. 2009, p. 17.

[5] Kelecy, T., and Jah, M., "Analysis of High Area-to-Mass Ratio (HAMR) GEO Space Object Orbit Determination and Prediction Performance: Initial Strategies to Recover and Predict HAMR GEO Trajectories with No A Priori Information," *Acta Astronautica*, Vol. 69, Nos. 7–8, 2011, pp. 551–558. doi:10.1016/j.actaastro.2011.04.019

[6] Kelecy, T., Jah, M., and DeMars, K., "Application of a Multiple Hypothesis Filter to Near GEO High Area-to-Mass Ratio Space Objects State Estimation," *Acta Astronautica*, Vol. 81, No. 2, 2012, pp. 435–444. doi:10.1016/j.actaastro.2012.08.006

[7] Linares, R., Crassidis, J. L., Jah, M. K., and Kim, H., "Astrometric and Photometric Data Fusion for Resident Space Object Orbit, Attitude, and Shape Determination Via Multiple-Model Adaptive Estimation," *AIAA Guidance, Navigation, and Control Conference*, Curran Associates Incorporated, Toronto, Ontario, Canada, Paper 2010-8341, Aug. 2010.

[8] Ziebart, M., "Generalized Analytical Solar Radiation Pressure Modeling Algorithm for Spacecraft of Complex Shape," *Journal of Spacecraft and Rockets*, Vol. 41, No. 5, 2004, pp. 840–848. doi:10.2514/1.13097

[9] Ashikhmin, M., and Shirley, P., "An Anisotropic Phong BRDF Model," *Journal of Graphics Tools*, Vol. 5, No. 2, 2000, pp. 25–32. doi:10.1080/10867651.2000.10487522

[10] Cook, R. L., and Torrance, K. E., "A Reflectance Model for Computer Graphics," *ACM Transactions on Graphics*, Vol. 1, No. 1, Jan. 1982, pp. 7–24. doi:10.1145/357290.357293

[11] Schlick, C., "An Inexpensive BRDF Model for Physically-Based Rendering," *Computer Graphics Forum*, Vol. 13, No. 3, 1994, pp. 233–246. doi:10.1111/cgf.1994.13.issue-3

[12] Gautschi, W., and Cahill, W. F., "Exponential Integral and Related Functions," *Handbook of Mathematical Functions With Formulas, Graphs, and Mathematical Tables*, edited by Abramowitz, M., and Stegun, I. A., National Bureau of Standards Applied Mathematics Series, Washington, DC, 1964, p. 272.

[13] Knocke, P. C., Ries, J. C., and Tapley, B. D., "Earth Radiation Pressure Effects on Satellites," *Proceedings of the AIAA/AAS Astrodynamics Conference*, Minneapolis, MN, Paper 88-4292-CP, Aug. 1988, pp. 577–587.

[14] McCarthy, J. J., and Martin, T. V., "A Computer Efficient Model of Earth Albedo Satellite Effects," NASA Goddard Space Flight Center, Planetary Sciences Dept., Rept. 012-77, 1977.

[15] Rakhmanov, E. A., Saff, E. B., and Zhou, Y. M., "Minimal Discrete Energy on the Sphere," *Mathematical Research Letters*, Vol. 1, No. 6, 1994, pp. 647–662.

[16] Saff, E. B., and Kuijlaars, A. B. J., "Distributing Many Points on a Sphere," *The Mathematical Intelligencer*, Vol. 19, No. 1, 1997, pp. 5–11. doi:10.1007/BF03024331

[17] Marshall, J. A., and Luthke, S. B., "Modeling Radiation Forces Acting on Topex/Poseidon for Precision Orbit Determination," *Journal of Spacecraft and Rockets*, Vol. 31, No. 1, 1994, pp. 99–105. doi:10.2514/3.26408

[18] Vallado, D. A., *Fundamentals of Astrodynamics and Applications*, 3rd ed., McGraw–Hill, New York, 2007, pp. 574–578.

[19] Shuster, M. D., "A Survey of Attitude Representations," *Journal of the Astronautical Sciences*, Vol. 41, No. 4, Oct.–Dec. 1993, pp. 439–517.

Downloaded by AFRL/DII on January 22, 2014 | http://arc.aiaa.org | DOI: 10.2514/1.60577

View publication stats